



## Supplementary Materials for

### **A Terradynamics of Legged Locomotion on Granular Media**

Chen Li, Tingnan Zhang, Daniel I. Goldman\*

\*Corresponding author. E-mail: [daniel.goldman@physics.gatech.edu](mailto:daniel.goldman@physics.gatech.edu)

Published 22 March 2013, *Science* **339**, 1408 (2013)

DOI: 10.1126/science.1229163

#### **This PDF file includes:**

- Materials and Methods
- Supplementary Text
- Figs. S1 to S14
- Tables S1 to S4
- References (34–38)
- Captions for Movies S1 to S6
- Caption for Additional Data Table S5

#### **Other Supplementary Material for this manuscript includes the following:**

(available at [www.sciencemag.org/cgi/content/full/339/6126/1408/DC1](http://www.sciencemag.org/cgi/content/full/339/6126/1408/DC1))

- Movies S1 to S6
- Additional Data Table S5 (.xls file)

## Materials and Methods

### Force measurements

We used aluminum to construct the plate element (area  $A = 3.81 \times 2.54 \text{ cm}^2$ , thickness = 0.64 cm) and model legs (maximal length  $2R = 7.62 \text{ cm}$ , width = 2.54 cm, thickness = 0.64 cm). We measured the friction coefficient  $\mu$  between aluminum and poppy seeds to be 0.40 (later we constructed robot legs using plastic of a similar friction coefficient with poppy seeds, 0.36), by placing an aluminum plate on a wooden plate bonded with a single layer of poppy seeds, increasing the slope of the wooden plate from zero, and examining the angle  $\xi$  at which the aluminum plate began to slide. Thus  $\mu = \tan \xi$ . The length and width of both the plate element and model legs were  $\sim 10$  times the particle diameter, ensuring that the granular media could be approximated as a continuum.

Before each force measurement, we used an air fluidized bed ( $24 \times 22 \text{ cm}^2$  surface area) (26) to prepare the granular media (15 cm deep) to a well-defined compaction (see table S1 for the volume fractions of closely and loosely packed states of the granular media tested). Air flow was turned off during force measurements. We used a 6 degree-of-freedom robotic arm (CRS Robotics) to move the plate element and rotate the model legs. We used a 6-axis force and torque transducer (ATI Industrial Automation) mounted between the intruder and the robotic arm to measure forces to a precision of 0.05 N at a sampling frequency of 100 Hz. We performed all the force measurements at low speeds ( $\sim 1 \text{ cm/s}$ ) to ensure that particle inertia was negligible, and in a vertical plane at the middle of the air fluidized bed and far from the sidewalls (distance  $> 3 \text{ cm}$ ) to minimize boundary effects.

In the plate element intrusion experiment, we attached the plate to the force and torque transducer via a supporting rod and an adjustable mount with which attack angle  $\beta$  could be varied. We varied intrusion angle  $\gamma$  by adjusting the trajectory of the robotic arm. For each combination of  $\beta$  and  $\gamma$ , we separately measured the forces on the supporting rod and mount moving in the granular media without the plate, and subtracted them to obtain forces exerted by the granular media on the plate alone.

During each test session, we first prepared the granular media while the plate was above the surface. We then moved the plate (oriented at attack angle  $\beta$ ) downward to the surface (depth  $|z| = 0$ ), paused it for 2 seconds, and then intruded it into the granular media along intrusion angle  $\gamma$ . After intrusion was finished, we prepared the granular media again, and extracted the plate along the same path. This gave us measurements of stresses  $\sigma_{z,x}$  for both  $\pm(\beta, \gamma)$ . For horizontal movements ( $\gamma = 0$ ),  $\sigma_{z,x}$  were nearly constant when the plate was far from the container sidewalls, and we obtained  $\alpha_{z,x}$  by fitting Eq. 1 to averages of  $\sigma_{z,x}$  in the steady state regions at three depths ( $|z| = 2.54 \text{ cm}$ ,  $5.08 \text{ cm}$ , and  $7.62 \text{ cm}$ ). We measured  $\alpha_{z,x}$  for  $\gamma$  within  $[-\pi/2, \pi/2]$ , and determined  $\alpha_{z,x}$  for  $\gamma$  within  $[-\pi, -\pi/2]$  and  $[\pi/2, \pi]$  by symmetry:

$$\begin{cases} \alpha_z(\beta, \gamma) = \alpha_z(-\beta, -\pi - \gamma) & \text{if } -\pi \leq \gamma \leq -\pi/2 \\ \alpha_z(\beta, \gamma) = \alpha_z(-\beta, \pi - \gamma) & \text{if } \pi/2 \leq \gamma \leq \pi \end{cases} \quad (\text{S1})$$

$$\begin{cases} \alpha_x(\beta, \gamma) = -\alpha_x(-\beta, -\pi - \gamma) & \text{if } -\pi \leq \gamma \leq -\pi/2 \\ \alpha_x(\beta, \gamma) = -\alpha_x(-\beta, \pi - \gamma) & \text{if } \pi/2 \leq \gamma \leq \pi \end{cases} \quad (\text{S2})$$

In the model leg rotation experiment, we rotated the model legs at an angular velocity  $\omega = 0.2 \text{ rad/s}$  at a hip height  $h = 2 \text{ cm}$  within leg angle  $-3\pi/4 \leq \theta \leq 3\pi/4$  (at the beginning

and end of which all three legs tested were fully above the granular surface), where leg angle  $\theta$  was defined as the angle sweeping from the vertical downward direction to the direction along which leg length was maximal. For each model leg, we separately measured the forces due to the weight of the model legs rotating in the air, and subtracted them to obtain the forces on the model legs exerted by the granular media during rotation.

Due to the high repeatability of our fluidized bed and robotic arm, we found that for all media tested, run-to-run variation in  $\alpha_{z,x}$  for fixed  $\beta$  and  $\gamma$  was always within  $0.005 \text{ N/cm}^3$  at any given depth; thus we only performed one trial for each combination of  $\beta$  and  $\gamma$ . All the stresses were calculated in the regions where the plate was far from the container boundaries (distance  $> 6 \text{ cm}$ ). We also confirmed that for low enough speeds, intrusion forces in granular media were insensitive to speed (for example, in loosely packed poppy seeds, at  $v = 1 \text{ m/s}$ , force only increased by less than 20% from that at  $v = 1 \text{ cm/s}$ ); thus, particle inertia was negligible.

### Robot experiments

We built our robot (body length = 13 cm, body mass = 150 g) by modifying a small commercially available robot (RoboXplorer, Smart Lab). The robot had similar morphology and kinematics as a RHex robot, with a rigid body and six legs performing 1 degree-of-freedom rotation in an alternating tripod gait. We substituted the stock motor with a stronger one (RadioShack Super Speed 9–18 VDC Hobby Motor, Model # 273-256) and modified the gear trains (gear ratio: 47 revolutions in the motor transmits into 1 rotation of the legs). These changes increased maximal stride frequency  $f$  to 5 Hz. We removed the external body shell to reduce weight and the belly area (to  $13 \times 2 \text{ cm}^2$ ). This reduced drag on the belly during locomotion on granular media.

We used 3-D printing to make custom robot legs. All the legs had the same maximal length  $2R' = 4.1 \text{ cm}$ , width = 1.0 cm, and thickness = 0.3 cm, but different curvatures  $1/r = [-1, -0.92, -0.60, 0, 0.60, 0.92, 1]/R'$ . The ABS plastic used to fabricate the legs had a similar friction coefficient with poppy seeds (0.36) to that of aluminum with poppy seeds (0.40). The leg width and length were  $\sim 10$  times the particle diameter, allowing the granular media to be approximated as a continuum. We ensured that the legs had large enough stiffness and moved like rigid bodies ( $< 5\%$  deformation) during locomotion.

We tuned the center of mass of the robot to overlap with the geometric center of the body by adding mass to the lighter end of the robot. We measured the masses, dimensions, and relative positions of all robot body and leg parts, and calculated the moment of inertia of the robot to be  $I = 2.08 \times 10^3 \text{ g cm}^2$  about the pitch axis through the center of mass. We powered the robot by an external power supply (Power Ten Inc.) to ensure constant voltage during trials, and adjusted voltage to vary stride frequency  $f$  between trials.

Before each trial, we used an air fluidized bed track ( $200 \times 50 \text{ cm}^2$  surface area) to prepare the granular media (12 cm deep) to a well-defined compaction, using methods similar to those in (21). We used two synchronized high-speed cameras (X-PRI, AOS Technologies) to capture top and side views of the robot's locomotion at 500 frame/s. We measured  $f$  from the side view, and measured forward speed  $v_x$  from the top view by digitizing a high contrast marker placed near the center of mass. For each  $f$  and  $1/r$ , we performed three trials and reported mean  $\pm$  s.d. for average forward speed  $\bar{v}_x$  in experiment.

### Robot simulation

We used a multibody dynamic simulator, MBDyn (34), to create a simulation of the robot locomotion on granular media. MBDyn features a full three-dimensional simulation with 6 degrees of freedom (3 translations and 3 rotations). We constructed the robot body using 3 rigid plates (the front, rear, and belly surfaces) and 6 rigid legs. We constrained the robot body movement within the vertical plane, with fore-aft and dorso-ventral translations and pitch, and allowed the legs to only rotate about their axes perpendicular to the vertical plane. For each time step, we calculated the depth  $|z|_s$ , attack angle  $\beta_s$ , and intrusion angle  $\gamma_s$  for each element to determine element stresses  $\sigma_{z,x}$  (using Eq. 1 and  $\alpha_{z,x}$  interpolated from the data in Fig. 2, C and D). We then summed forces on all elements to obtain net forces  $F_{z,x}$  using our resistive force model by Eq. 2, and calculated the body dynamics by Eq. 3. We found that dividing each body plate and leg into fewer elements could further increase simulation speed at the cost of model accuracy.

In simulation tests, we varied curvature  $1/r$  between  $-1/R' \leq 1/r \leq 1/R'$  in increments of  $0.04/R'$ , and varied stride frequency  $f$  between  $0 \leq f \leq 5$  Hz in increments of 0.2 Hz. For each  $f$  and  $1/r$ , we performed three trials using different initial conditions with a phase difference of  $2\pi/3$  for each tripod. We found that this resulted in variation in average forward speed  $\bar{v}_x$  of  $\ll 1$  cm/s; thus, we reported only the means of  $\bar{v}_x$  in simulation. We confirmed that at the maximal stride frequency tested (5 Hz) the leg speeds were  $< 1$  m/s averaged over a stance, allowing particle inertia to be negligible.

## Supplementary Text

This supplementary text contains 5 sections:

In section 1, we review the depth-only vertical penetration and horizontal drag force models. Based on the flat-plate approximation, we then calculate stresses per unit depth and net forces on rotating legs using these depth-only force models, and compare with our resistive force measurements and model predictions.

In section 2, we present our resistive force measurements and model calculations for a variety of granular media tested, which have different particle size, density, friction, and compaction; from these results we discover that the stress profiles are generic.

In section 3, we develop a scaling routine to capture the similar stress profiles observed for the variety of granular media, by scaling generic stress profiles determined from averages of fits to the measured stress profiles. This provides a practical means to easily apply our resistive force model.

In section 4, we test the ability of our scaling routine to predict forces on intruders moving in natural sands, and discuss limitations of our model for natural sands.

In section 5, we compare the predictive accuracy for locomotor performance (speed) of the robot using our resistive force model to that using our scaling routine and that using the depth-only force models.

## 1. Depth-only force models and their limitations

Previous studies of intrusion forces in granular media focused on simple intruders (e.g. plates, rods, and spheres) moving with simple kinematics (e.g. vertical penetration and horizontal drag). For example, the vertical force  $f_z$  on a horizontal plate element ( $\beta = 0$ ) moving vertically ( $\gamma = \pm\pi/2$ ) in granular media was observed to be proportional to the plate's depth  $|z|$  and area  $A$  (21, 35):

$$f_z = \alpha_z(0, \text{sgn}(\dot{z})\pi/2)|z|A \quad (\text{S3})$$

Similarly, the horizontal force  $f_x$  on a vertical plate element ( $\beta = \pm\pi/2$ ) moving horizontally ( $\gamma = 0$ ) in granular media was proportional to plate depth  $|z|$  and plate area  $A$  (36–38):

$$f_x = \alpha_x(\pi/2, 0)|z|A \quad (\text{S4})$$

where  $\dot{z}$  is the velocity of the plate in the vertical direction, and  $\alpha_z(0, \text{sgn}(\dot{z})\pi/2)$  and  $\alpha_x(\pi/2, 0)$  are vertical and horizontal stresses per unit depth for  $(\beta, \gamma) = (0, \pm\pi/2)$  and  $(\pm\pi/2, 0)$  (determined from measurements in Fig. 2, C and D).

Both the vertical penetration and horizontal drag force models only account for the dependence of stresses on the intruder's depth ( $|z|$ ), but not the dependence on its orientation (attack angle  $\beta$ ) or movement direction (intrusion angle  $\gamma$ ). Hereafter we refer to these force models as the “depth-only force models”.

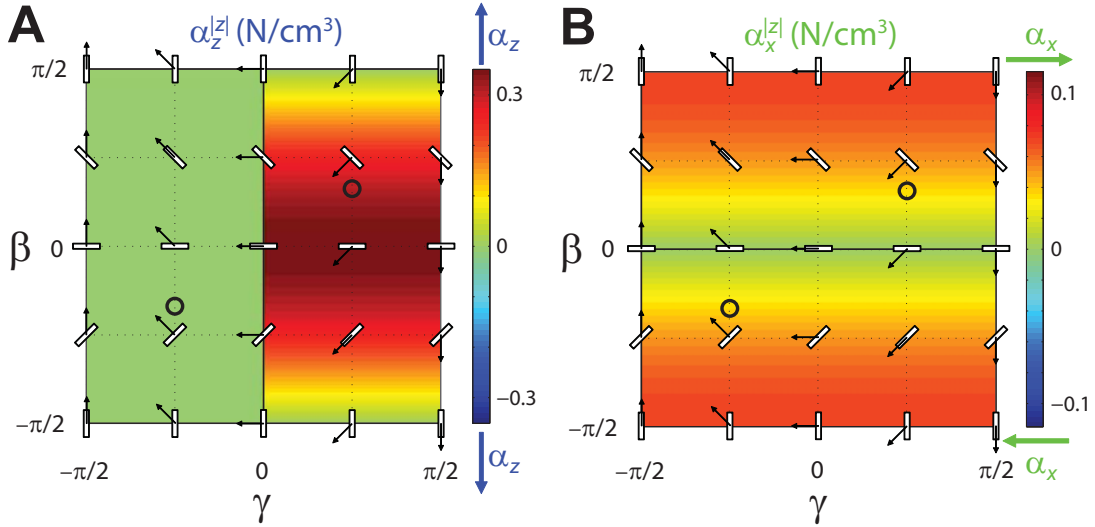


FIG. S1. Effective vertical ( $\alpha_z^{[z]}(\beta, \gamma)$ , left) and horizontal ( $\alpha_x^{[z]}(\beta, \gamma)$ , right) stresses per unit depth as a function of attack angle  $\beta$  and intrusion angle  $\gamma$  for loosely packed poppy seeds, calculated from eq. S7 using  $\alpha_z(0, \text{sgn}(\dot{z})\pi/2)$  and  $\alpha_x(\pi/2, 0)$  measured in experiment (Fig. 2, C and D). See Fig. 2, A and B for schematic of the experiment and definition of variables.

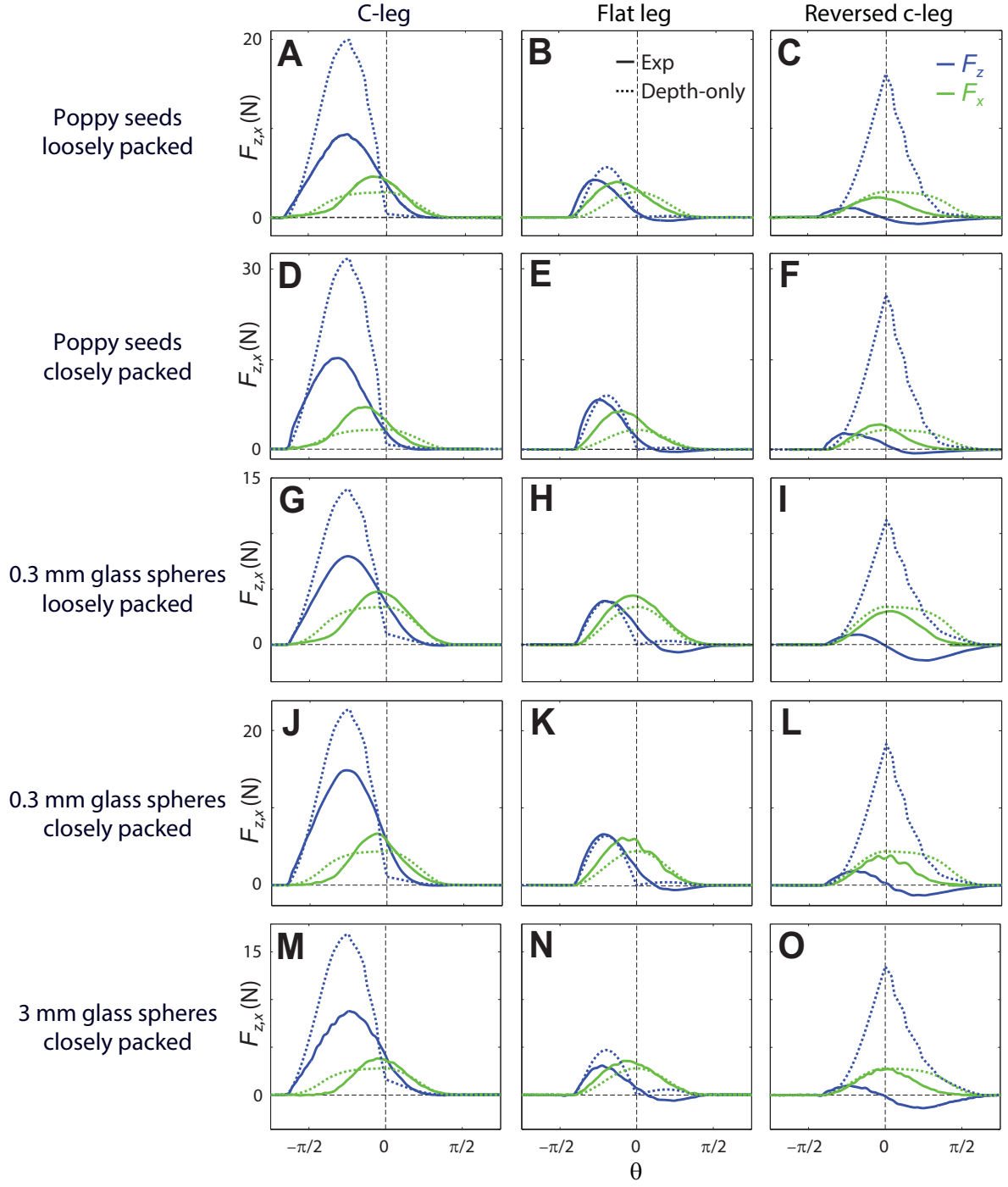


FIG. S2. Net lift  $F_z$  (blue) and thrust  $F_x$  (green) versus leg angle  $\theta$  on the three model legs for all media tested. Solid curves: experimental measurements. Dotted curves: predictions from the depth-only force models. See Fig. 3 A to C for schematic of the experiment and definition of variables.

In previous studies of legged locomotion on granular media (16, 21, 37), due to the lack of the resistive force model, the forces on a complex intruder were estimated from the depth-only force models, using the flat-plate approximation: The vertical force on a leg element of area  $dA_s$  and arbitrary  $\beta$  and  $\gamma$  was approximated by that on a horizontal leg element whose area was the element area projected into the horizontal plane (16, 21):

$$dA_{zs} = |\cos\beta|dA_s \quad (\text{S5})$$

Similarly, the horizontal force on the leg element was approximated by that on a vertical leg element whose area was the element area projected into the vertical plane (37):

$$dA_{xs} = |\sin\beta|dA_s \quad (\text{S6})$$

The effective stresses per unit depth calculated from these depth-only force models using flat plate approximation were then:

$$\begin{cases} \alpha_z^{(|z|)}(\beta, \gamma) = \alpha_z(0, \text{sgn}(\dot{z})\pi/2)|\cos\beta| \\ \alpha_x^{(|z|)}(\beta, \gamma) = \alpha_x(\pi/2, 0)|\sin\beta| \end{cases} \quad (\text{S7})$$

Comparing the  $\alpha_{z,x}^{(|z|)}(\beta, \gamma)$  calculated using eq. S7 (fig. S1) to our resistive force measurements  $\alpha_{z,x}(\beta, \gamma)$  (Fig. 2, C and D) for loosely packed poppy seeds, we found that these depth-only force models did not capture most of the measured stress profiles. In particular, the depth-only vertical penetration force model overpredicted  $\alpha_z(\beta, \gamma)$  for all  $\beta$  and  $\gamma$  except when the plate was horizontal ( $\beta = 0$ ) and moving vertically ( $\gamma = \pm\pi/2$ ). Contrary to experimental measurements, the  $\alpha_{z,x}^{(|z|)}$  calculated from the depth-only models were symmetric to  $\beta = 0$  (horizontal orientation), and  $\alpha_z^{(|z|)}$  (or  $\alpha_x^{(|z|)}$ ) was always opposing the plate's vertical (or horizontal) velocity (the shaded regions shrank to a line).

We used these depth-only force models to calculate the net lift  $F_z$  and thrust  $F_x$  versus leg angle  $\theta$  for the three model legs rotated through all media tested, by the integration of stresses over the legs (Eq. 3) using  $\alpha_{z,x}^{(|z|)}(\beta, \gamma)$ . We found that they not only significantly overpredicted peak  $F_z$  (by up to 1400%) but also erroneously predicted similar peak  $F_{z,x}$  for the c-leg and reversed c-leg (fig. S2).



## 2. Generality of resistive force model for a variety of granular media

To test the generality of our resistive force model and provide a database for future studies (we provide the force measurements in this section in Additional Data Table S5), we performed resistive force measurements for three granular media—poppy seeds, 0.3 mm glass spheres, and 3 mm glass spheres (fig. S3), which have different particle size, shape, density, and friction (measured by angle of repose) (table S1). We prepared these granular media into well-defined compactions which affected stresses (21, 38). We prepared poppy seeds and 0.3 mm glass spheres into both a loosely packed (LP) and a closely packed (CP) states, and prepared 3 mm glass spheres into a closely packed (CP) state (table S1).

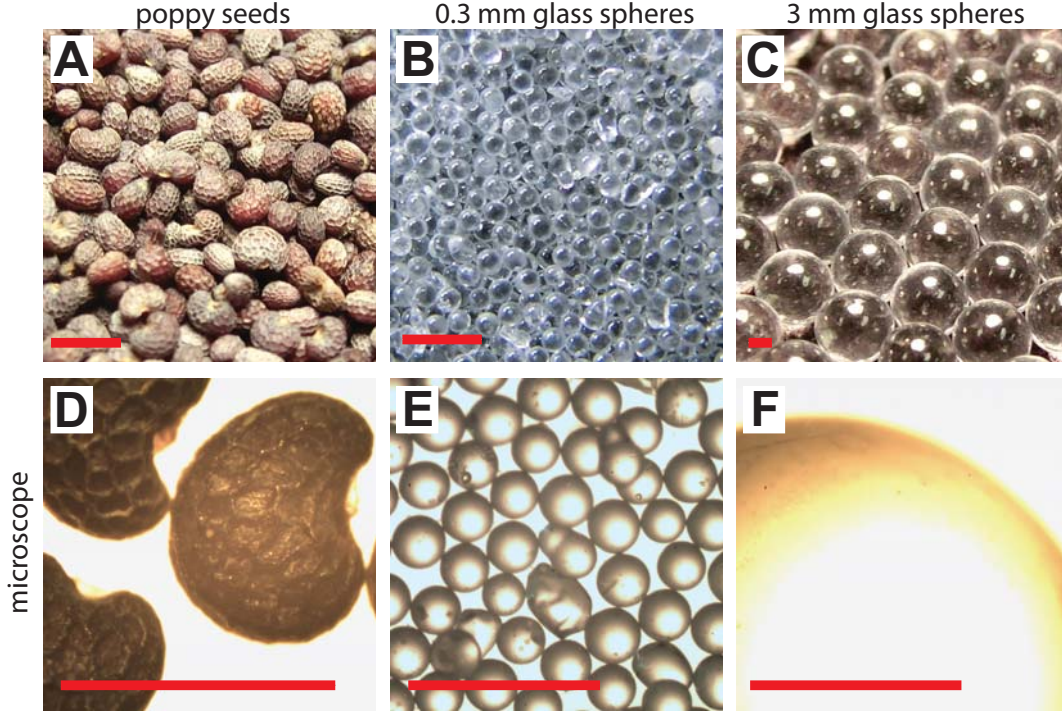


FIG. S3. The three granular media tested in our study. Top: regular images. Bottom: microscope images. The length of each scale bar is 1 mm. Photo credit of (A) and (C): Sarah Sharpe.

TABLE S1. Physical properties of the three granular media (in different compactions) for which resistive forces were measured. \*Angle of repose for 3 mm glass spheres courtesy of Sarah Sharpe.

granular medium	particle diameter (mm)	particle material density (g/cm <sup>3</sup> )	compaction	volume fraction	angle of repose (°)
poppy seeds	$0.7 \pm 0.2$	1.1	loosely packed (LP)	0.58	36
			closely packed (CP)	0.62	47
0.3 mm glass spheres	$0.27 \pm 0.04$	2.5	loosely packed (LP)	0.58	25
			closely packed (CP)	0.62	35
3 mm glass spheres	$3.2 \pm 0.2$	2.6	closely packed (CP)	0.63	21*

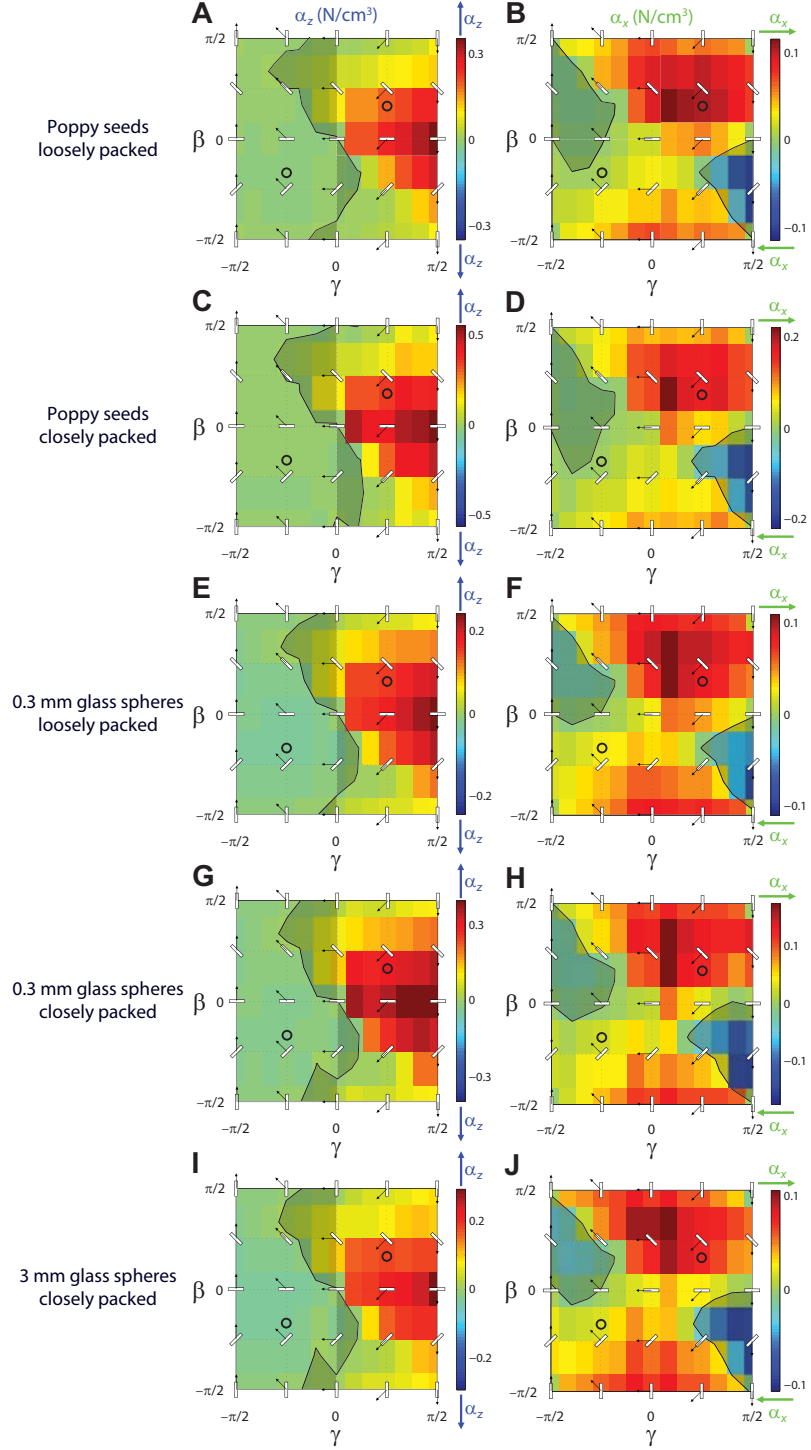


FIG. S4. Vertical ( $\alpha_z^{[z]}(\beta, \gamma)$ , left) and horizontal ( $\alpha_{z,x}^{[z]}(\beta, \gamma)$ , right) stresses per unit depth as a function of attack angle  $\beta$  and intrusion angle  $\gamma$  for all media tested. (A) and (B) are reproduced from Fig. 2, C and D. See Fig. 2, A and B for schematic of the experiment and definition of variables.

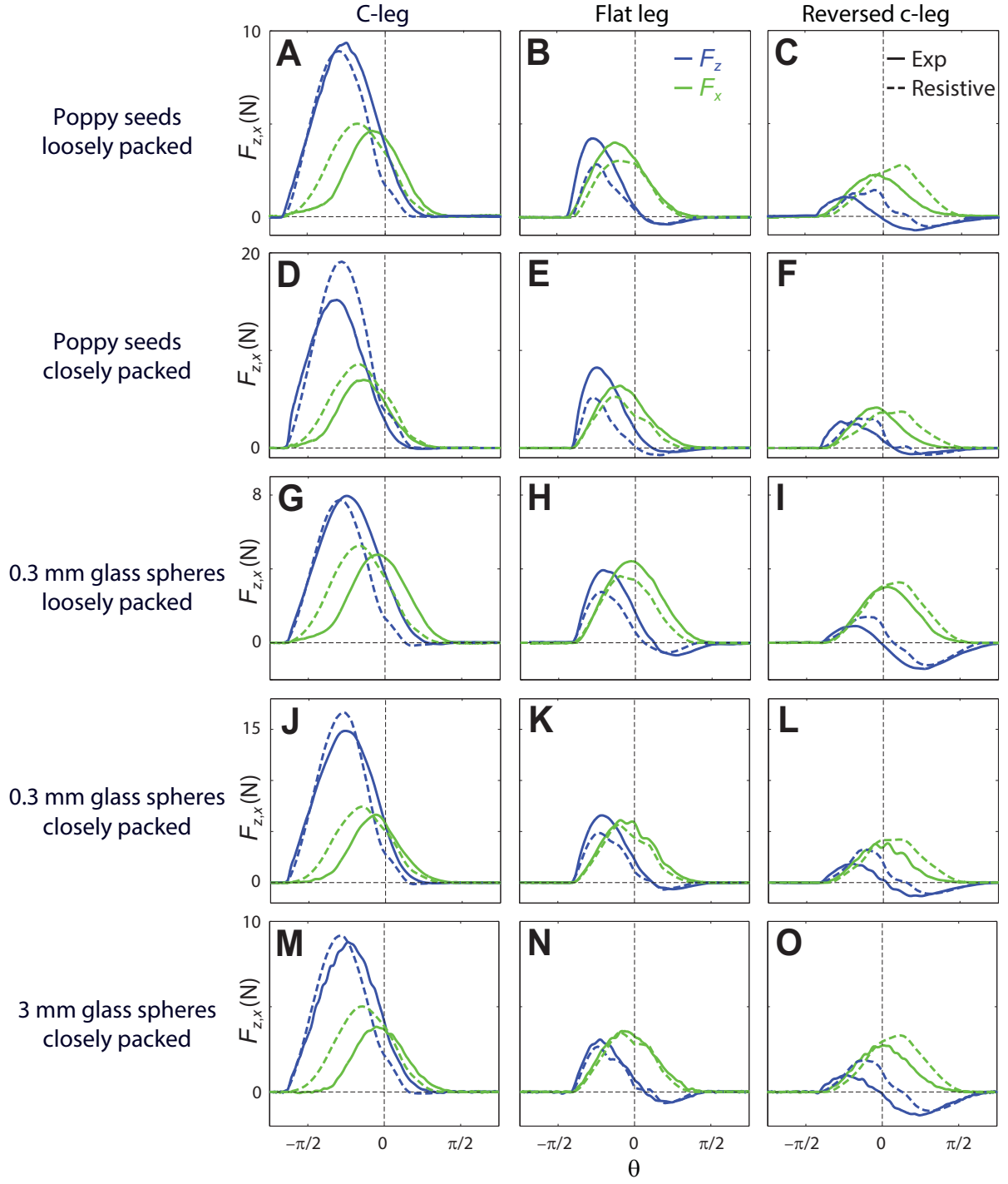


FIG. S5. Net lift  $F_z$  (blue) and thrust  $F_x$  (green) versus leg angle  $\theta$  on the three model legs for all media tested. Solid curves: experimental measurements. Dashed curves: resistive force model predictions. (A) to (C) are reproduced from Fig. 3, D to F. See Fig. 3 A to C for schematic of the experiment and definition of variables.

Despite differences in magnitudes and fine features, we observed similar profiles of the vertical and horizontal stresses per unit depth  $\alpha_{z,x}(\beta, \gamma)$  for all media tested (fig. S4). We provide the  $\alpha_{z,x}(\beta, \gamma)$  data for all media in Additional Data Table S5 (separate file in Microsoft Excel format).

For all media tested, our resistive force model predicted the net lift  $F_z$  and thrust  $F_x$  versus leg angle  $\theta$  on the three model legs rotated through granular media (fig. S5). Compared with predictions from the depth-only force models (fig. S1), our resistive force model had a significant improvement in accuracy.

### 3. Scaling routine for easy use of the resistive force model

To provide a means for practical use of our resistive force model and comparison with new theories of dense granular flow (32), we performed a fitting approximation to the stress per unit depth data  $\alpha_{z,x}$  for all media tested, and developed a scaling routine based on the data fits.

We first performed a discrete Fourier transform of the  $\alpha_{z,x}(\beta, \gamma)$  data (fig. S4) over  $-\pi/2 \leq \beta \leq \pi/2$  and  $-\pi \leq \gamma \leq \pi$  to obtain a fitting function. We examined the Fourier coefficients and found that the  $\alpha_{z,x}(\beta, \gamma)$  data of all media tested could be well approximated by the following fits:

$$\begin{cases} \alpha_z^{\text{fit}}(\beta, \gamma) = \sum_{m=-1}^1 \sum_{n=0}^1 [A_{m,n} \cos 2\pi(\frac{m\beta}{\pi} + \frac{n\gamma}{2\pi}) + B_{m,n} \sin 2\pi(\frac{m\beta}{\pi} + \frac{n\gamma}{2\pi})] \\ \alpha_x^{\text{fit}}(\beta, \gamma) = \sum_{m=-1}^1 \sum_{n=0}^1 [C_{m,n} \cos 2\pi(\frac{m\beta}{\pi} + \frac{n\gamma}{2\pi}) + D_{m,n} \sin 2\pi(\frac{m\beta}{\pi} + \frac{n\gamma}{2\pi})] \end{cases} \quad (\text{S8})$$

using nine zeroth- and first-order terms (whose magnitudes are larger than  $0.05A_{0,0}$ ) (table S2):

$$M = (A_{0,0} \ A_{1,0} \ B_{1,1} \ B_{0,1} \ B_{-1,1} \ C_{1,1} \ C_{0,1} \ C_{-1,1} \ D_{1,0})^T \quad (\text{S9})$$

TABLE S2. Zeroth- and first-order Fourier coefficients  $M$  (in  $\text{N}/\text{cm}^3$ ) for all media tested. These coefficients are  $> 0.05A_{0,0}$ .  $M_0$  is a generic coefficient curve to which the  $M$  for each granular medium can be collapsed onto by division of a scaling factor  $\zeta$  ( $\zeta = 1$  for  $M_0$ ). We choose the magnitudes of  $M_0$  such that for all media tested the values of  $\zeta$  are nearly the same as the values of  $\alpha_z^{\text{fit}}(0, \pi/2)$  (this becomes useful later in the scaling routine). CP and LP indicates closely packed and loosely packed states.

granular medium	poppy seeds		0.3 mm glass spheres		3 mm glass spheres	generic coefficients
compaction	LP	CP	LP	CP	CP	n/a
matrix notation	$M_{\text{poppyLP}}$	$M_{\text{poppyCP}}$	$M_{0.3\text{mmLP}}$	$M_{0.3\text{mmCP}}$	$M_{3\text{mmCP}}$	$M_0$
$A_{0,0}$	0.051	0.094	0.040	0.081	0.045	0.206
$A_{1,0}$	0.047	0.092	0.030	0.063	0.031	0.169
$B_{1,1}$	0.053	0.092	0.045	0.078	0.046	0.212
$B_{0,1}$	0.083	0.151	0.077	0.133	0.084	0.358
$B_{-1,1}$	0.020	0.035	0	0.024	0.012	0.055
$C_{1,1}$	-0.026	-0.039	-0.031	-0.050	-0.031	-0.124
$C_{0,1}$	0.057	0.086	0.066	0.087	0.060	0.253
$C_{-1,1}$	0	0.018	0	0	0	0.007
$D_{1,0}$	0.025	0.046	0.017	0.033	0.015	0.088
scaling factor $\zeta$	0.248	0.488	0.194	0.371	0.214	1

By symmetry,  $\alpha_z(\beta \leq 0, \pi/2) = \alpha_z(\beta \geq 0, \pi/2)$ , and  $\alpha_x(\beta \leq 0, \pi/2) = -\alpha_x(\beta \geq 0, \pi/2)$ . However, the data slightly deviated from this equality because the initial positions of the

plate were close to one of the boundaries of the container. Therefore, before the Fourier transform, we averaged the raw data for  $\gamma = \pm\pi/2$  to restore symmetry by  $\alpha_z(\beta \leq 0, \pi/2) = \alpha_z(\beta \geq 0, \pi/2) = \frac{1}{2}[\alpha_z(\beta \leq 0, \pi/2) + \alpha_z(\beta \geq 0, \pi/2)]$ . The raw data were also not uniformly sampled in the  $\gamma$  direction; we found that this only resulted in small errors in data fitting.

We found that for all media tested (denoted by  $i = \text{poppyLP, poppyCP, 0.3mmLP, 0.3mmCP, and 3mmCP}$ ), the Fourier coefficients  $M_i$  could be collapsed onto a generic coefficient curve,  $M_0$ , by dividing  $M_i$  by a scaling factor  $\zeta_i$  (table S2, fig. S6):

$$M_i/\zeta_i \approx M_0 \quad (\text{S10})$$

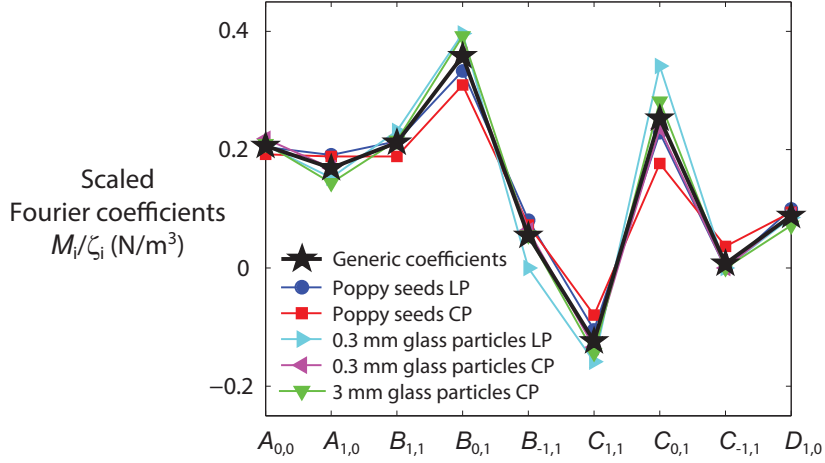


FIG. S6. Scaled Fourier coefficients  $M_i/\zeta_i$  of all media tested (thin colored curves) can be approximated by a generic coefficient curve  $M_0$  (thick black curve).

This enabled us to scale stresses per unit depth ( $\alpha_{z,x}$ ) and thus forces ( $f_{z,x}$  and  $F_{z,x}$ ) for all media tested. By eq. S8, using the generic coefficient curve  $M_0$  ( $\zeta = 1$ ) from table S2, we calculated generic stress (per unit depth) profiles  $\alpha_{z,x}^{\text{generic}}(\beta, \gamma)$  (fig. S7). We found that, by multiplication by the scaling factor  $\zeta$ , these generic stress profiles well approximated the measured  $\alpha_{z,x}(\beta, \gamma)$  (fig. S4) for all media tested:

$$\alpha_{z,x}(\beta, \gamma) \approx \zeta \alpha_{z,x}^{\text{generic}}(\beta, \gamma) \quad (\text{S11})$$

Using Eq. 2 and  $\alpha_{z,x}^{\text{generic}}(\beta, \gamma)$ , we calculated the generic force profiles  $F_{z,x}^{\text{generic}}(\theta)$  on the three model legs rotated through granular media (fig. S8). We found that in all media tested and for both the c-leg and the flat leg, these generic force profiles captured the measured  $F_{z,x}$  scaled by the scaling factors  $\zeta$ :

$$F_{z,x}^{\text{generic}}(\theta) \approx F_{z,x}(\theta)/\zeta \quad (\text{S12})$$

However, the agreement was worse for the reversed c-leg. Our resistive force model revealed that this was because by using  $F_{z,x}^{\text{generic}}(\theta)$ , stresses were significantly overestimated for the reversed c-leg's elements that reached large depths.

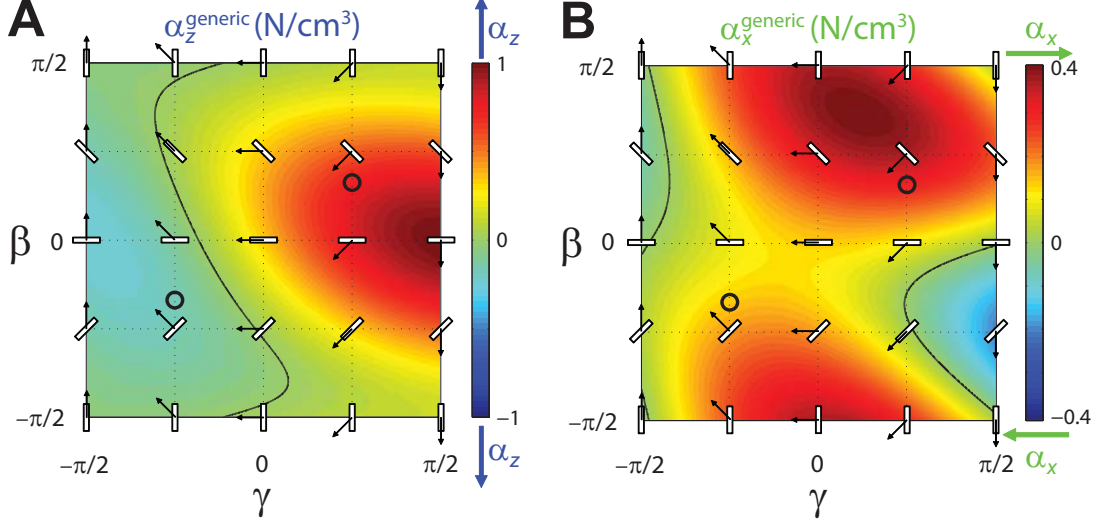


FIG. S7. Generic stress (per unit depth) profiles  $\alpha_{z,x}^{\text{generic}}(\beta, \gamma)$  for all media tested. See Fig. 2, A and B for schematic of the experiment and definition of variables.

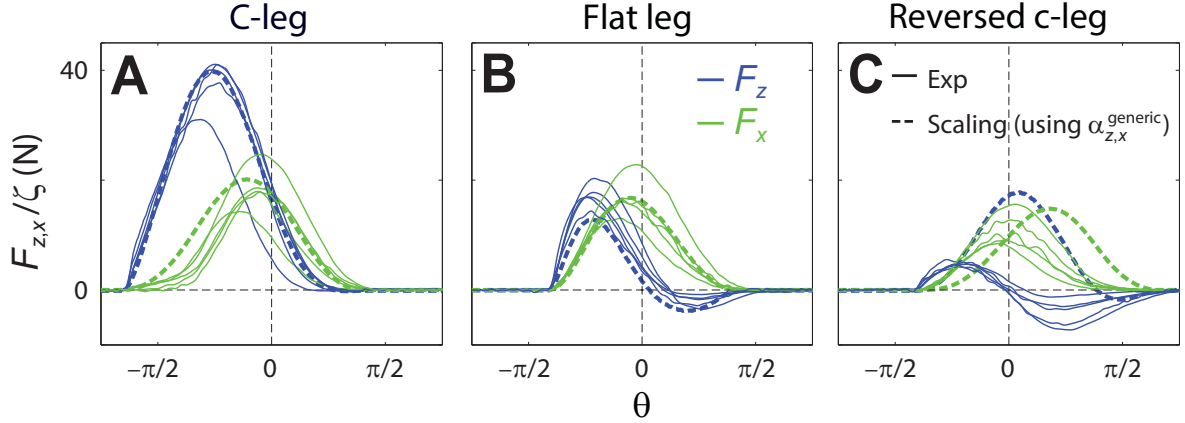


FIG. S8. The measured net forces scaled by the measured scaling factors  $F_{z,x}(\theta)/\zeta$  for all media tested (thin curves), in comparison with the generic profiles of net forces  $F_{z,x}^{\text{generic}}(\theta)$  (thick curves) calculated from the generic stress profiles  $\alpha_{z,x}^{\text{generic}}$  (fig. S7). See Fig. 3 A to C for schematic of the experiment and definition of variables.

We further observed that the ratio of the maximal vertical stress (which occurred on a horizontal plate moving downward) between the measurements ( $\alpha_z(0, \pi/2)$ ) and fits ( $\alpha_z^{\text{fit}}(0, \pi/2)$ ) was similar for all media tested (table S3):

$$\chi = \alpha_z(0, \pi/2) / \alpha_z^{\text{fit}}(0, \pi/2) = 1.26 \pm 0.14 \quad (\text{S13})$$

where  $\chi$  is in mean  $\pm$  s.d.

TABLE S3. Comparison of the measurements and fits of maximal vertical stress per unit depth (in N/cm<sup>3</sup>) for all media tested. CP and LP indicates closely packed and loosely packed states.

granular medium	poppy seeds		0.3 mm glass spheres		3 mm glass spheres
compaction	LP	CP	LP	CP	CP
$\alpha_z(0, \pi/2)$	0.35	0.56	0.24	0.40	0.29
$\alpha_z^{\text{fit}}(0, \pi/2)$	0.26	0.47	0.19	0.38	0.22
$\chi = \alpha_z(0, \pi/2)/\alpha_z^{\text{fit}}(0, \pi/2)$	1.37	1.19	1.27	1.05	1.33

Therefore, we propose that for a sufficiently level and uniform dry granular medium composed of near-monodispersed, near-spherical, rounded particles of  $\sim 0.1$  to  $\sim 1$  mm in diameter, one can simply measure its maximal vertical stress  $\alpha_z(0, \pi/2)$  by pushing a horizontal plate downward to infer the maximal value of the fit vertical stress  $\alpha_z^{\text{fit}}(0, \pi/2)$ :

$$\alpha_z^{\text{fit}}(0, \pi/2) = \alpha_z(0, \pi/2)/\chi \approx 0.8\alpha_z(0, \pi/2) \quad (\text{S14})$$

The value of  $\alpha_z^{\text{fit}}(0, \pi/2)$  in N/m<sup>3</sup> then gives the scaling factor  $\zeta$  for this granular medium, because we choose the magnitudes of the generic curve  $M_0$  so that the values of  $\zeta$  and  $\alpha_z^{\text{fit}}(0, \pi/2)$  are nearly the same for all media tested:

$$\zeta \approx \alpha_{z,x}^{\text{fit}}(\beta, \gamma) \quad (\text{S15})$$

Note that this equation only equates the numeric values on both sides, because  $\zeta$  is dimensionless.

Then, from eq. S11, by scaling the generic stress profiles  $\alpha_{z,x}^{\text{generic}}$  (fig. S7) by the determined scaling factor  $\zeta$ , we can obtain an approximation of stress profiles for this granular medium:

$$\alpha_{z,x}(\beta, \gamma) \approx \alpha_{z,x}^{\text{scaled}}(\beta, \gamma) = \zeta \alpha_{z,x}^{\text{generic}}(\beta, \gamma) \quad (\text{S16})$$

This scaling routine provides an alternative to measuring  $\alpha_{z,x}$  for all  $\beta$  and  $\gamma$  (at the cost of model accuracy). As demonstrated by the model leg rotation experiments (fig. S8) and robot locomotion experiments (see fig. S13 in the next section), our scaling routine only suffers a small loss in accuracy for much of the leg morphology and stride frequencies tested. This technique can be particularly useful in a field setting, because only a single force measurement is needed.

We summarize these practical steps to use our resistive force model in fig. S9.



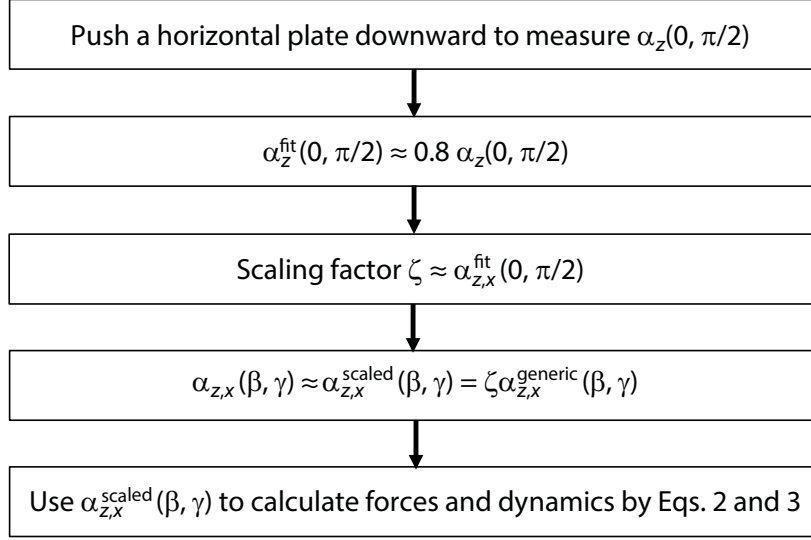


FIG. S9. A scaling routine to easily apply our resistive force model.

#### 4. Applicability of resistive force model to natural sands

To test the predictive power of our resistive force model for natural sands, we chose two natural sands of higher polydispersity and angularity than those of the granular media tested, and examined whether the scaling routine (fig. S9) could predict the net forces  $F_{z,x}(\theta)$  on the three model legs during rotation through the natural sands.

The two natural sands, referred to as “Yuma sand” and “29 Palms sand” (table S4, fig. S10), were collected from the Mojave Desert in the southwest United States, one from Yuma, Arizona and the other from 29 Palms, California. The Yuma sand had most particles (70% by mass) in the 0.06–0.3 mm particle size range, and the 29 Palms sand had most particles (91% by mass) in the 0.3–3 mm particle size range. Both natural sands were fluidized by the fluidized bed before each force measurement was performed. We further tested modified 29 Palms sand with reduced polydispersity to examine the effect of polydispersity on model accuracy.

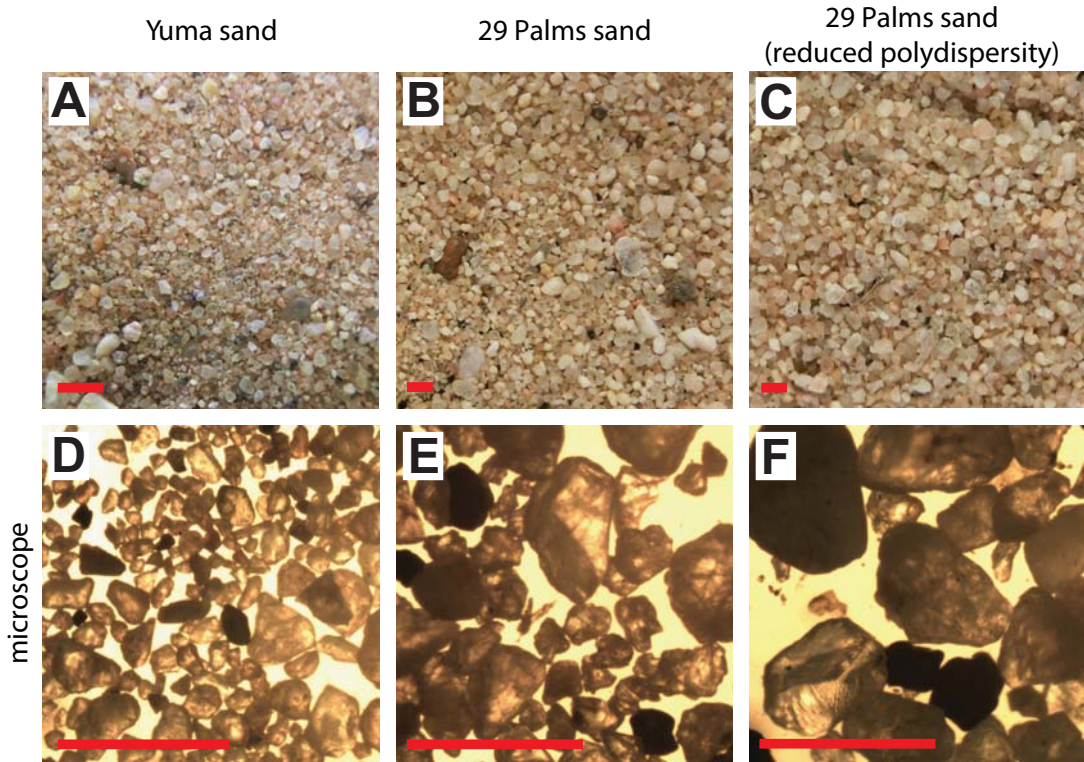


FIG. S10. The natural sands used to test the predictive power of our scaling routine. Top: regular images. Bottom: microscope images. The length of each scale bar is 1 mm.

During downward penetration ( $\gamma = \pi/2$ ) into both the Yuma and 29 Palms sands, the vertical stress  $\sigma_z$  on a horizontal plate ( $\beta = 0$ ) increased nearly proportionally to depth  $|z|$  at low enough depths (fig. S11, solid curves), similar to observations in the granular media tested. However, for both the natural sands,  $\sigma_z$  versus  $|z|$  displayed nonlinearity as depth further increased sooner than observed for the granular media tested. This was because both natural sands had larger internal stresses (larger  $\alpha_{z,x}$  magnitudes) and likely suffered

TABLE S4. Particle size distribution of the natural sands tested.

natural sand	particle diameter (mm)	mass percentage (%)
Yuma sand	< 0.06	2
	0.06–0.3	68
	0.3–3.0	17
	>3.0	13
29 Palms sand	< 0.3	5
	0.3–0.6	36
	0.6–0.7	55
	0.7–3.0	3
	>3.0	1
29 Palms sand (reduced polydispersity)	0.6–0.7	100

boundary effects at much shallower depths as compared to the granular media tested. In addition, for the Yuma sand which had more particles in the 0.06–0.3 mm particle size range, this nonlinearity due to boundary effects was more pronounced. Therefore, to minimize possible errors from boundary effects, we perform linear fits with zero intercept to the  $\sigma_z$  versus  $|z|$  data (fig. S11, dashed curves) over the linear regime (0–2 cm for the Yuma sand; 0–3 cm for the 29 Palms sand) to obtain  $\alpha_z(0, \pi/2)$  (slopes of dashed lines) for both the natural sands. This gave us their scaling factors  $\zeta$  and estimates of their stress profiles from  $\alpha_{z,x}^{\text{scaled}}(\beta, \gamma) = \zeta \alpha_{z,x}^{\text{generic}}(\beta, \gamma)$  (eq. S16).

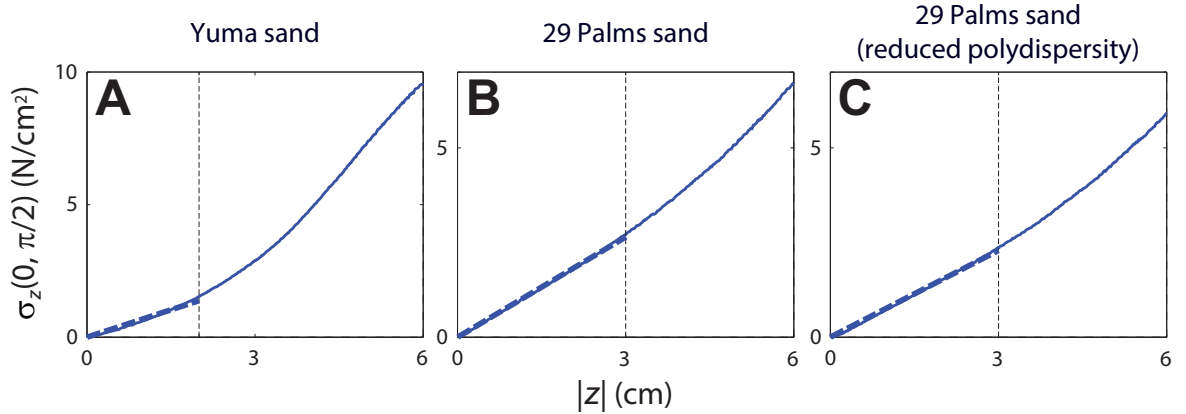


FIG. S11. Maximal vertical stress  $\sigma_z(0, \pi/2)$  versus depth  $|z|$  measured in the natural sands using a plate element horizontally oriented and penetrating vertically downward ( $\beta = 0, \gamma = \pi/2$ ). Dashed lines are linear fits with zero intercept to the data in the linear regime at shallow depths. See Fig. 2, A and B for schematic of the experiment and definition of variables.

For the three model legs rotated through both the Yuma and 29 Palms sands, both the net lift  $F_z$  and thrust  $F_x$  versus leg angle  $\theta$  displayed asymmetric profiles similar to those observed for the granular media tested (fig. S12, solid curves). Using the  $\alpha_z(0, \pi/2)$  obtained from the vertical penetration experiment (fig. S11), our scaling routine significantly overpredicted

$F_{z,x}(\theta)$  on the c-leg for both the Yuma and 29 Palms sands (both by 35%). Nevertheless, the shape of model predictions were similar to experimental observations (fig. S12, dashed curves). The model accuracy was best for the flat leg, and worst for the reversed c-leg.

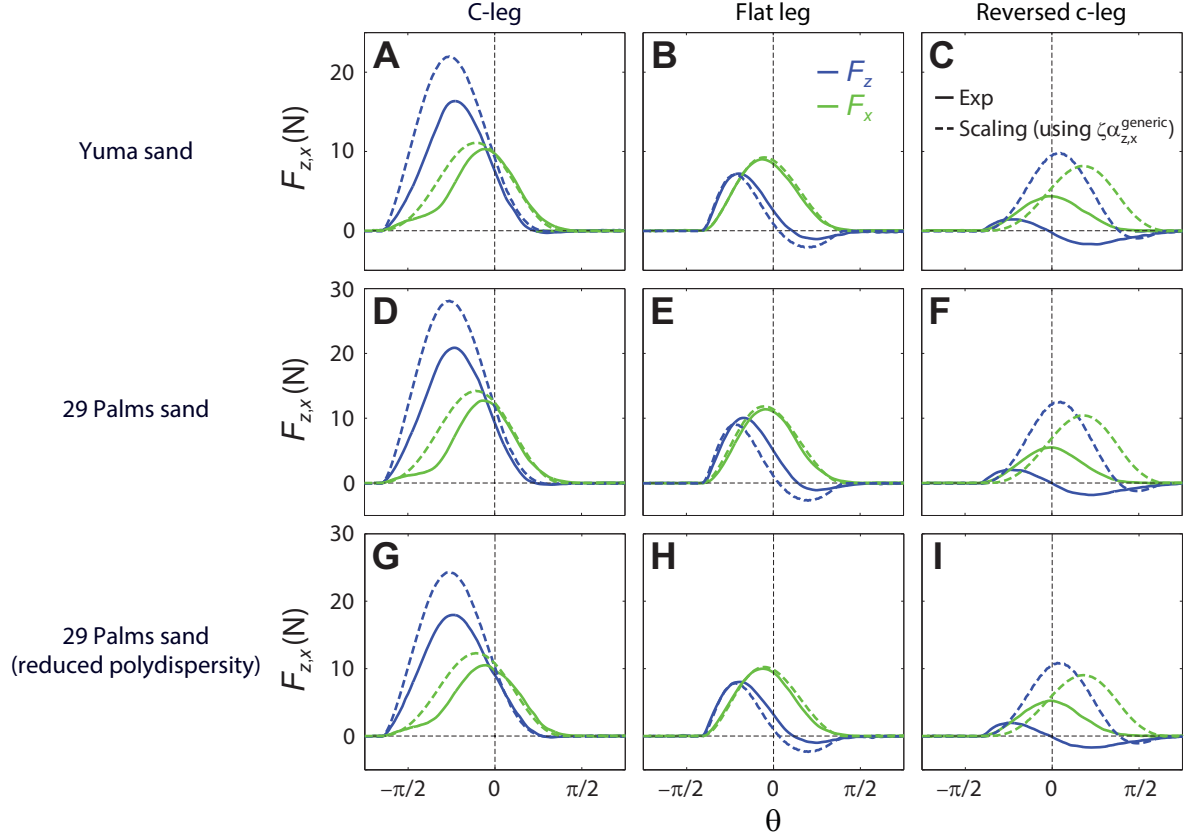


FIG. S12. Net lift  $F_z$  (blue) and thrust  $F_x$  (green) versus leg angle  $\theta$  on the three model legs for the natural sands tested. Solid curves: experimental measurements. Dashed curves: resistive force model predictions using the scaling routine (fig. S9). See Fig. 3 A to C for schematic of the experiment and definition of variables.

There are two major differences between the natural sands and the granular media tested: The natural sands have higher polydispersity, and are also less spherical and more angular. To probe where the overprediction (of forces on the c-leg) stemmed from, we further tested the 29 Palms sand with reduced polydispersity (obtained by sieving the sand to obtain only the 0.6–0.7 mm particles). We found that while both  $\alpha_z(0, \pi/2)$  and  $F_{z,x}(\theta)$  dropped by 14% (figs. S11 and S12), the model overprediction of forces on the c-leg remained the same (35%). This suggested that the non-spherical and angular shape of the natural sand particles, rather than their higher polydispersity, was likely the cause of the model overprediction.

## 5. Comparison of model accuracy in predicting legged locomotion

To evaluate the accuracy of our scaling routine in predicting legged locomotion, we used our multibody dynamic simulation to simulate the robot's movement on loosely packed poppy seeds using the scaled generic stress profiles ( $\alpha_{z,x}^{\text{scaled}} = \zeta \alpha_{z,x}^{\text{generic}}$ ). We calculated the robot's average forward speed  $\bar{v}_x$  versus stride frequency  $f$  and leg curvature  $1/r$  (fig. S13), and compare it with experimental measurements and resistive force model predictions (without using the scaling routine). As a comparison, we also calculated  $\bar{v}_x(f, 1/r)$  using  $\alpha_{z,x}^{|z|}$  obtained from the depth-only force models (fig. S1).

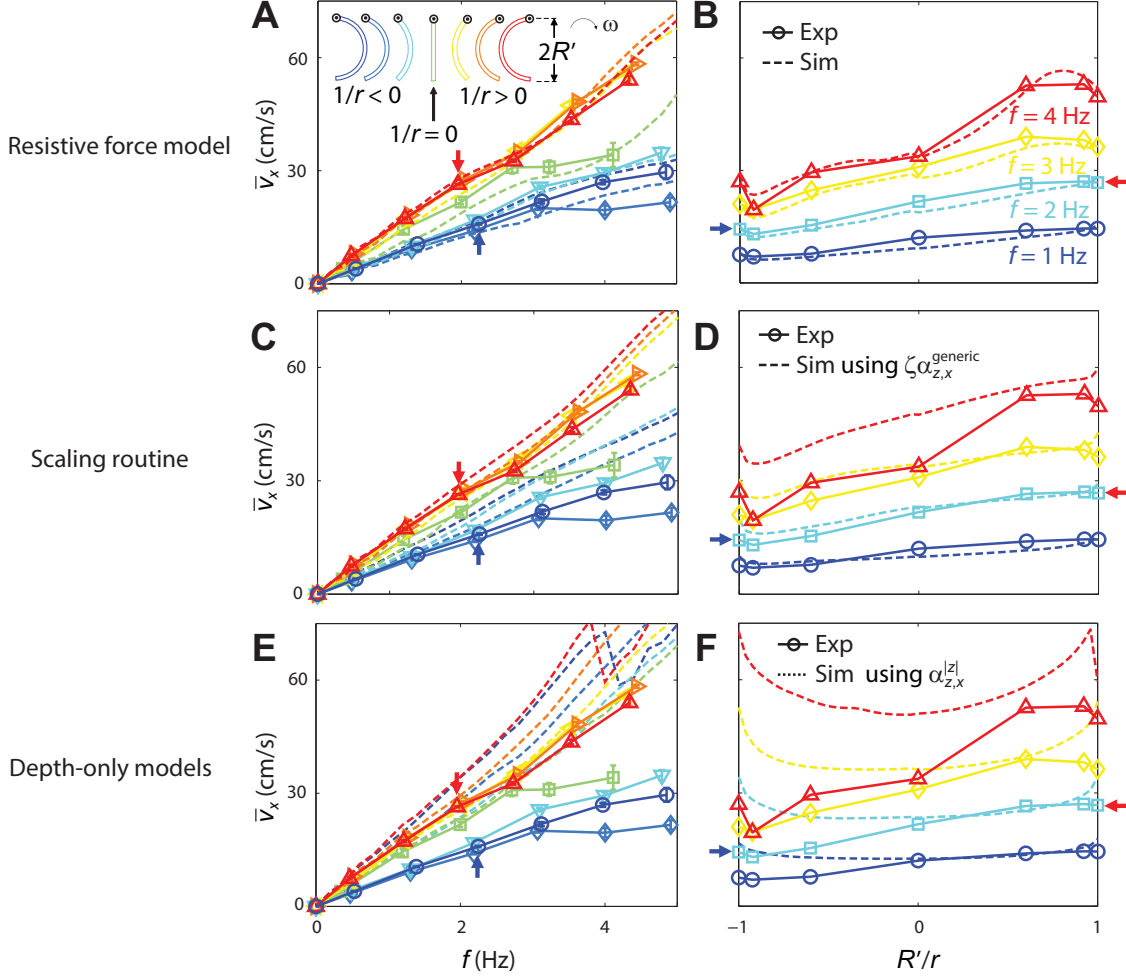


FIG. S13. Average forward speed  $\bar{v}_x$  of the robot as a function of stride frequency  $f$  (left) and leg curvature  $1/r$  (right) on loosely packed poppy seeds. Solid curves: experimental measurements. Dashed curves: simulation predictions. Top: using the measured stresses ( $\alpha_{z,x}$ ). Middle: using the scaled generic stress profiles ( $\alpha_{z,x}^{\text{scaled}} = \zeta \alpha_{z,x}^{\text{generic}}$ ). Bottom: using stresses from the depth-only force models ( $\alpha_{z,x}^{|z|}$ ). The drop of  $\bar{v}_x$  vs.  $f$  at near  $R'/r = 1$  using  $\alpha_{z,x}^{|z|}$  was due to pitch instability of the robot in simulation (the robot became upside down). (A) and (B) are reproduced from Fig. 4, C and D. See Fig. 4 A and B for representative runs of the experiment and definition of variables.

We found that the simulation using scaled generic stress profiles ( $\zeta\alpha_{z,x}^{\text{generic}}$ ) only suffered a small loss in accuracy as compared to that using the measured  $\alpha_{z,x}$ . By contrast, the simulation using stresses  $\alpha_{z,x}^{|z|}$  from the depth-only force models suffered a larger loss in accuracy (by up to 150% error), and in particular, erroneously predicted that the robot moved at similar speeds using both c-legs and reversed c-legs.

In addition to the predictions locomotor kinematics, our resistive force model and multi-body dynamic simulation also allowed us to calculate ground reaction forces (fig. S14) during locomotion on granular media (which would be otherwise difficult to measure), in a similar fashion as calculations of lift, drag, thrust, traction, and resistance in studies of vehicle mobility in fluids and terramechanics studies. Notice the larger vertical ground reaction forces produced by the C-legs relative to those by the reversed c-legs. This allowed the robot to maintain higher lift above the granular medium, reducing drag on the belly.

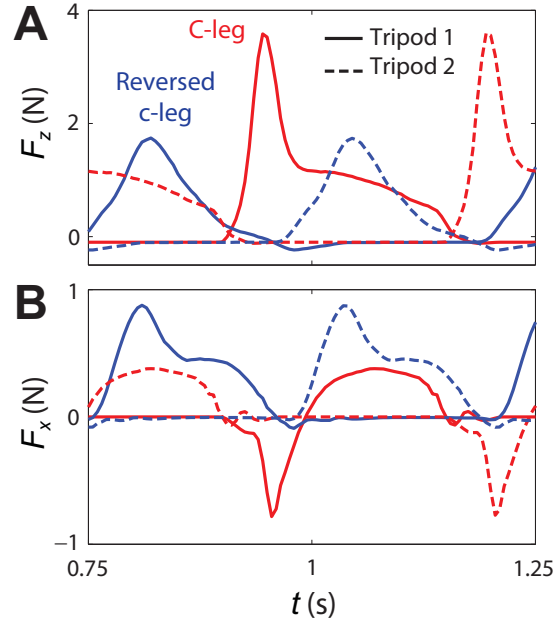


FIG. S14. Vertical ( $F_z$ , top) and horizontal ( $F_x$ , bottom) ground reaction forces versus time  $t$  on both tripods of the robot during locomotion on loosely packed poppy seeds, calculated from the simulation using the resistive force model. Solid and dashed curves correspond to forces on the two tripods of legs, respectively. Results are for the two representative runs shown in Fig. 4B. Note that these ground reaction forces do not include those on the robot body (which were also calculated but not plotted here).

### Movie S1

Plate element intrusion experiments. Left: Intrusion for representative attack angle and intrusion angle  $(\beta, \gamma) = (\pi/6, \pi/4)$ . Right: Extraction for representative  $(\beta, \gamma) = -(\pi/6, \pi/4)$ . Top: Videos of the plate moving in a granular medium (loosely packed poppy seeds). Bottom: Vertical ( $\sigma_z$ , blue curve) and horizontal ( $\sigma_x$ , green curve) stresses versus depth  $|z|$ . Videos were taken with the plate at the container boundary for illustration purpose only. Forces were measured with the plate in the middle of the container, far away from the boundary. The red lines originating from the center of the top panels indicate granular forces on the plate element. The plate was moved at 1 cm/s. See Fig. 2, A and B for schematic of the experiment and definition of variables.

### Movie S2

Leg rotation experiments. Left: C-leg. Right: Reversed c-leg. Top: Videos of the leg rotating through a granular medium (loosely packed poppy seeds). Bottom: Net lift ( $\sigma_z$ , blue curve) and thrust ( $\sigma_x$ , green curve) versus leg angle  $\theta$ . Videos were taken with the plate at the container boundary for illustration purpose only. Forces were measured with the plate in the middle of the container, far away from the boundary. The red lines originating from the center of the top panels indicate granular forces on the model legs. The model legs were rotated at 0.2 rad/s (leg tip speed  $\sim 1$  cm/s). Note that in the c-leg video the axle deflected slightly during rotation—this was an artifact due to the extra-long supporting rod in order for the plate to reach the boundary for illustration purpose only. For force measurements performed in the middle of the container, the supporting rod was shorter and the axle did not deflect. See Fig. 3 A to C for schematic of the experiment and definition of variables.

### Movie S3

Leg rotation model calculations. Left: C-leg. Right: Reversed c-leg. Top: Videos of the leg rotating through a granular medium (loosely packed poppy seeds). Bottom: Net lift ( $\sigma_z$ , blue curve) and thrust ( $\sigma_x$ , green curve) versus leg angle  $\theta$ . The thick red lines originating from the center of the top panels indicate net forces on the model legs. The thin red lines on the model legs indicate element forces (on a larger scale). See Fig. 3 A to C for schematic of the experiment and definition of variables.

### Movie S4

Robot (body length = 13 cm, body mass  $m = 150$  g) running on a granular medium (loosely packed poppy seeds) using c-legs and stride frequency  $f = 5$  Hz. Video is played in real time.

### Movie S5

Robot experiments. Top: Using c-legs ( $f = 2.0$  Hz). Middle: Using reversed c-legs ( $f = 2.2$  Hz). Bottom: Forward speed  $v_x$  versus time  $t$ . Videos are played 5 times slower than real time. Note that in the trial using reversed c-legs, the robot body orientation was reversed; we verified that this did not affect robot kinematics and speed (because the center of mass of the robot was tuned to overlap with the geometric center of the body). See Fig. 4 A for definition of variables.

## Movie S6

Robot simulation. Top: Using c-legs ( $f = 2.0$  Hz). Middle: Using reversed c-legs ( $f = 2.2$  Hz). Bottom: Forward speed  $v_x$  versus time  $t$ . Videos are played 5 times slower than real time. The red and green arrows on the two tripod of legs indicate the ground reaction forces on the leg elements calculated from simulation. Note that the forces on the body are not shown. See Fig. 4 A for definition of variables.

## Additional Data Table S5 (separate file in Microsoft Excel format)

Original data of vertical ( $\alpha_z$ ) and horizontal ( $\alpha_x$ ) stresses per unit depth versus attack angle  $\beta$  and intrusion angle  $\gamma$ , for all media tested. These data were used to produce Fig. 2, C and D and fig. S4.



## References and Notes

1. M. H. Dickinson *et al.*, *Science* **288**, 100 (2000).
2. M. G. Bekker, *Off-the-Road Locomotion, Research and Development in Terramechanics* (Univ. of Michigan Press, Ann Arbor, MI, 1960).
3. B. Etkin, *Dynamics of Atmospheric Flight* (Wiley, New York, 1972).
4. J. N. Newman, *Marine Hydrodynamics* (MIT Press, Cambridge, MA, 1977).
5. S. Vogel, *Life in Moving Fluids: The Physical Biology of Flow* (Princeton Univ. Press, Princeton, NJ, 1996).
6. E. Lauga, T. R. Powers, The hydrodynamics of swimming microorganisms. *Rep. Prog. Phys.* **72**, 096601 (2009). [doi:10.1088/0034-4885/72/9/096601](https://doi.org/10.1088/0034-4885/72/9/096601)
7. Z. J. Wang, Dissecting insect flight. *Annu. Rev. Fluid Mech.* **37**, 183 (2005). [doi:10.1146/annurev.fluid.36.050802.121940](https://doi.org/10.1146/annurev.fluid.36.050802.121940)
8. C. J. Pennycuik, Mechanics of flight. *Avian Biol.* **5**, 1 (1975).
9. G. V. Lauder, J. C. Nauen, E. G. Drucker, Experimental hydrodynamics and evolution: Function of median fins in ray-finned fishes. *Integr. Comp. Biol.* **42**, 1009 (2002). [doi:10.1093/icb/42.5.1009](https://doi.org/10.1093/icb/42.5.1009) [Medline](#)
10. R. Dudley, *The Biomechanics of Insect Flight: Form, Function, Evolution* (Princeton Univ. Press, Princeton, NJ, 2002).
11. R. S. Fearing *et al.*, Wing transmission for a micromechanical flying insect. *IEEE Int. Conf. Rob. Auto.* **2000**, 1509 (2000).
12. G. V. Lauder, E. J. Anderson, J. Tangorra, P. G. A. Madden, Fish biorobotics: Kinematics and hydrodynamics of self-propulsion. *J. Exp. Biol.* **210**, 2767 (2007). [doi:10.1242/jeb.000265](https://doi.org/10.1242/jeb.000265) [Medline](#)
13. R. Blickhan, The spring-mass model for running and hopping. *J. Biomech.* **22**, 1217 (1989). [doi:10.1016/0021-9290\(89\)90224-8](https://doi.org/10.1016/0021-9290(89)90224-8) [Medline](#)
14. G. A. Cavagna, H. Thys, A. Zamboni, The sources of external work in level walking and running. *J. Physiol.* **262**, 639 (1976). [Medline](#)
15. P. Holmes, R. J. Full, D. E. Koditschek, J. Guckenheimer, The dynamics of legged locomotion: Models, analyses, and challenges. *SIAM Rev.* **48**, 207 (2006). [doi:10.1137/S0036144504445133](https://doi.org/10.1137/S0036144504445133)
16. C. Li, S. T. Hsieh, D. I. Goldman, Multi-functional foot use during running in the zebra-tailed lizard (*Callisaurus draconoides*). *J. Exp. Biol.* **215**, 3293 (2012). [doi:10.1242/jeb.061937](https://doi.org/10.1242/jeb.061937) [Medline](#)
17. L. R. Brand, Variations in salamander trackways resulting from substrate differences. *J. Paleontol.* **70**, 1004 (1996).
18. S. G. Fancy, R. G. White, Energy expenditures by caribou while cratering in snow. *J. Wildl. Manage.* **49**, 987 (1985). [doi:10.2307/3801384](https://doi.org/10.2307/3801384)

19. L. J. Vitt, S. S. Sartorius, T. C. S. Avila-Pires, M. C. Espósito, Life on the leaf litter: The ecology of *Anolis nitens tandai* in the Brazilian Amazon. *Copeia* **2001**, 401 (2001). [doi:10.1643/0045-8511\(2001\)001\[0401:LOTLLT\]2.0.CO;2](https://doi.org/10.1643/0045-8511(2001)001[0401:LOTLLT]2.0.CO;2)
20. M. Raibert, K. Blankespoor, G. Nelson, R. Playter, and the BigDog Team; BigDog, the rough-terrain quadruped robot. *Inter. Fed. Auto. Cont.* **2008**, 10822 (2008).
21. C. Li, P. B. Umbanhowar, H. Komsuoglu, D. E. Koditschek, D. I. Goldman, Sensitive dependence of the motion of a legged robot on granular media. *Proc. Natl. Acad. Sci. U.S.A.* **106**, 3029 (2009). [doi:10.1073/pnas.0809095106](https://doi.org/10.1073/pnas.0809095106) [Medline](#)
22. A. M. Johnson, M. T. Hale, G. C. Haynes, D. E. Koditschek, Autonomous legged hill and stairwell ascent. *2011 IEEE Saf. Sec. Res. Rob.* **2011**, 134 (2011).
23. T. Zhang *et al.*, *Int. J. Robotics. Res.* **32**, 10.1177/0278364913481690 (2013).
24. R. M. Nedderman, *Statics and Kinematics of Granular Materials* (Cambridge Univ. Press, New York, 1992).
25. G. Meirion-Griffith, M. Spenko, An empirical study of the terramechanics of small unmanned ground vehicles. *IEEE Aerospace Conf.* **2010**, 1 (2010).
26. R. D. Maladen, Y. Ding, C. Li, D. I. Goldman, Undulatory swimming in sand: Subsurface locomotion of the sandfish lizard. *Science* **325**, 314 (2009). [doi:10.1126/science.1172490](https://doi.org/10.1126/science.1172490) [Medline](#)
27. Y. Ding, N. Gravish, D. I. Goldman, Drag induced lift in granular media. *Phys. Rev. Lett.* **106**, 028001 (2011). [doi:10.1103/PhysRevLett.106.028001](https://doi.org/10.1103/PhysRevLett.106.028001) [Medline](#)
28. Materials and methods are available as supplementary materials on *Science* Online.
29. R. A. Bagnold, *The Physics of Blown Sand and Desert Dunes* (Dover Publications, Mineola, NY, 2005).
30. G. Cho, J. Dodds, J. C. Santamarina, Particle shape effects on packing density, stiffness, and strength: natural and crushed sands. *J. Geotech. Geoenviron. Eng.* **132**, 591 (2006). [doi:10.1061/\(ASCE\)1090-0241\(2006\)132:5\(591\)](https://doi.org/10.1061/(ASCE)1090-0241(2006)132:5(591))
31. B. Chaudhuri, A. Mehrotra, F. J. Muzzio, M. S. Tomassone, Cohesive effects in powder mixing in a tumbling blender. *Powder Technol.* **165**, 105 (2006). [doi:10.1016/j.powtec.2006.04.001](https://doi.org/10.1016/j.powtec.2006.04.001)
32. K. Kamrin, G. Koval, Nonlocal constitutive relation for steady granular flow. *Phys. Rev. Lett.* **108**, 178301 (2012). [doi:10.1103/PhysRevLett.108.178301](https://doi.org/10.1103/PhysRevLett.108.178301) [Medline](#)
33. J. A. Clack, *Gaining Ground: The Origin and Evolution of Tetrapods* (Indiana Univ. Press, Bloomington, IN, 2012).
34. G. L. Ghiringhelli, P. Masarati, P. Mantegazza, M. W. Nixon, Multi-body analysis of a tiltrotor configuration. *Nonlinear Dyn.* **19**, 333 (1999). [doi:10.1023/A:1008386219934](https://doi.org/10.1023/A:1008386219934)
35. G. Hill, S. Yeung, S. A. Koehler, Scaling vertical drag forces in granular media. *Europhys. Lett.* **72**, 137 (2005). [doi:10.1209/epl/i2005-10203-3](https://doi.org/10.1209/epl/i2005-10203-3)
36. R. Albert, M. A. Pfeifer, A.-L. Barabási, P. Schiffer, Slow drag in a granular medium. *Phys. Rev. Lett.* **82**, 205 (1999). [doi:10.1103/PhysRevLett.82.205](https://doi.org/10.1103/PhysRevLett.82.205)

37. N. Mazouchova, N. Gravish, A. Savu, D. I. Goldman, Utilization of granular solidification during terrestrial locomotion of hatchling sea turtles. *Biol. Lett.* **6**, 398 (2010). [doi:10.1098/rsbl.2009.1041](https://doi.org/10.1098/rsbl.2009.1041) [Medline](#)
38. N. Gravish, P. B. Umbanhowar, D. I. Goldman, Force and flow transition in plowed granular media. *Phys. Rev. Lett.* **105**, 128301 (2010). [doi:10.1103/PhysRevLett.105.128301](https://doi.org/10.1103/PhysRevLett.105.128301) [Medline](#)